Low Frequency Analysis of Radio Sources

A thesis submitted towards partial fulfilment of
BS-MS Dual Degree Programme

by

M. Dinesh Kumar

under the guidance of

Dr. Ramana Athreya

Associate Professor

Indian Institute of Science Education and Research
Pune

Certificate

This is to certify that this thesis entitled "Low Frequency Analysis of Radio Sources" submitted towards the partial fulfilment of the BS-MS dual degree programme at the Indian Institute of Science Education and Research Pune represents original research carried out by "M. Dinesh Kumar" at "Indian Institute Of Science Education And Research, Pune", under the supervision of "Dr. Ramana Athreya" during the academic year 2011-2012.

Student
M.Dinesh
Kumar

Supervisor
Dr. Ramana
Athreya

Acknowledgements

I express my deepest gratitude to Dr. Ramana Athreya for his patience and spending his valuable time in helping me grasp the fundamentals in the subject, without which this thesis wouldn't be possible. I would like to thank my lab mate Shadab Alam for the hours spent in debugging my code and for clarifying my doubts i had during the course of my work. I would also like to convey my special thanks to all my friends who helped me, bared me, and encouraged me throughout my college life.

Abstract

Radio sources emit high luminosity radiations in the radio regime. There are two types of radio sources: normal galaxies & radio galaxies. The radio emission from these galaxies arises from synchrotron emission. Generally the power-law is followed at high frequencies (from 300 MHz to 30 GHz) given by Flux density (S) $\sim \nu^{\alpha}$, where α is the spectral index, with a downward curvature (peak) in the spectrum below 300 MHz. Study of the spectra near this curvature helps us characterize the physical conditions in the plasma, both inside and outside the radio source.

In our study we planned to compare the low frequency spectra of normal galaxies and radio galaxies. Due to unavailability of 150 MHz data, it is difficult to do our low frequency spectra analysis. So, we attempted one another problem, where we did a low frequency analysis ($<$1000 MHz in rest frame) of redshift dependence on spectral index in powerful radio galaxies, within a specified luminosity range. In our analysis we found that spectral index is primarily correlated with redshifts (i.e. steeper spectra at higher redshifts) than with luminosity. We measured the spectral index difference between higher redshift ($z>2$) and lower redshift ($0.85<z<1.7$) sources at 300 MHz rest frame frequency, which came ~ 0.11. This value is ~ 0.1 which was obtained at 1 GHz rest frame by Athreya & Kapahi ([4]). Thus concluding that at least some of the difference in spectral index is due to steeper electron injection spectrum at high redshifts.

Contents

Chapter 1

Introduction

1.1 Radio Sources

Cosmic radio sources emit large amounts of their radiation at radio frequencies of the electromagnetic spectrum. There are two types of radio sources: normal galaxies in which the emission is faint and confined to the disk of the galaxy, and radio galaxies which typically exhibit double lobed structure powered by relativistic jets which transport energy from a super massive black-hole at the centre of the galaxy.
The brightness temperature in radio sources is much higher than any possible physical temperature expected in such sources. Therefore, it is believed that radio emission is non-thermal in nature and arises from the synchrotron mechanism. Unlike thermal emission where flux density increases with frequency (ν) in the Rayleigh-Jeans limit ($\nu \ll kT_B$), for synchrotron emitters flux density decreases with ν. Non-thermal radio sources are known to follow power-law spectra (Flux density S $\sim \nu^{\alpha}$,where α is the spectral index and lies between 0 and -2.5) at frequencies between 300 MHz and 30 GHz, with a downward curvature (peak) in the spectrum below 300 MHz.
Radio galaxies may be more than a million times more luminous than normal galaxies. Most of the radiation comes from extended lobes which can span upto several megaparsecs (1 megaparsec $\sim 3.08 \times 10^{22}$ m) from the host galaxy.

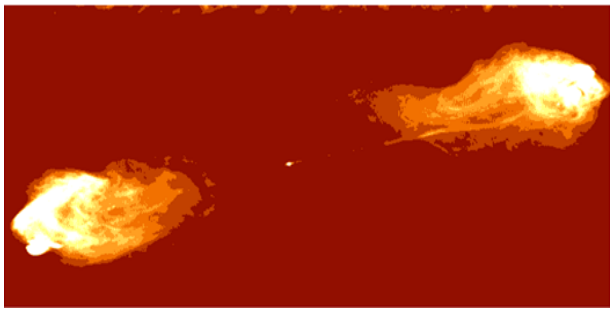

Figure 1.1: Image of a radio galaxy (Cygnus A) showing the double lobed structure. The host galaxy is coincident with the radio core seen as a compact spot at the centre. The lobes of the radio source extend on both sides of the radio core.

Radio emission from normal galaxies is believed to arise from supernova explosions and HII regions. They are much less luminous than radio galaxies and do not exhibit the double lobed structure of the latter.

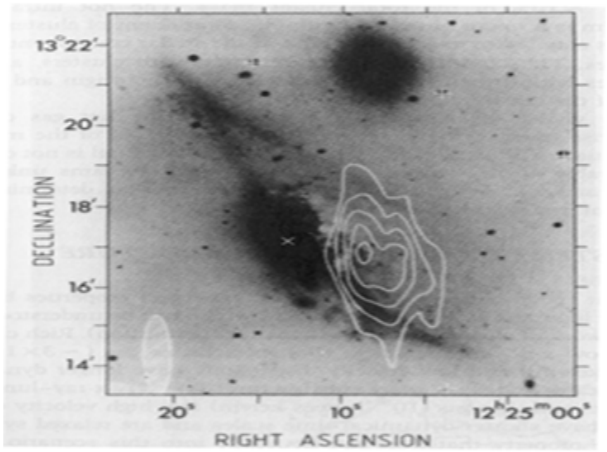

Figure 1.2: Contours of radio emission of the displaced disk of NGC 4438, superimposed on an optical image of the galaxy. Also in the picture (top) is the companion galaxy NGC 4435. The radio observations where made with the Westerbork Synthesis Radio Telescope at 1.4 GHz by C..Kotanyi and R. Ekers.

1.2 Synchrotron Theory

When a charged particle encounters a magnetic field, it gets accelerated and radiates energy. Under non-relativistic conditions (that is, when particle

velocities are much less than the speed of light), this cyclotron radiation is not strong enough to be of much astrophysical importance. However, if the particle is highly relativistic, it emits a broadband synchrotron radiation. For a single electron, the frequency near which this synchrotron emission is a maximum is called critical frequency(ν_c) and is defined as :

$$\nu_c = 3 \times e/(4\pi mc) \times B \times (E/(mc^2))^2 \tag{1.1}$$

where $3 \times e/(4\pi mc)$ is equal to 16.08 in practical units, ν_c is expressed in MHz, B is the perpendicular magnetic field measured in microgauss and E in meV.
Observationally, we see that synchrotron emission from an ensemble of electrons has a power-law spectrum. This can be explained if these electrons follow a power-law energy distribution given by N(E)=$\int n_0 E^{-\gamma} dE$. The relationship between γ, the energy index, and α, the spectral index, is given by, $\alpha = -(\gamma - 1)/2$.

1.3 Modification of Spectra from a power-law

Typically spectral index (α) is constant over a large range of frequencies. Most of the radio sources have spectral indices close to -0.75, though the range of values extend from 0 to -2.5. Spectral index can also vary with ν, in which case it is calculated by:

$$\alpha(\nu) = \partial logS/\partial log\nu \tag{1.2}$$

We discuss, below, some of the physical processes which result in a deviation of the spectrum from a power law. A schematic representation of this is shown in Fig. 1.3. Therefore, study of the spectra near this curvature can characterize the physical conditions in the plasma both inside and outside the radio source.

1.3.1 Electron Energy Cut-off

Naturally, any electron spectrum will have low energy cut-off (E_{low}) and high energy cut-off (E_{high}) to avoid infinities in the real world. This will result in departures from a power-law at frequencies corresponding to the electron energy cut-off. The frequencies (ν_{low} and ν_{high}) corresponding to these energy cut-offs can be obtained by substituting the value of E_{low} and E_{high} in eq 1.1. The spectral index below the low frequency cut-off is expected to be α = +0.3, and is expected to fall exponentially above high frequency cut-off.

1.3.2 Absorption Processes

The presence of absorption, either within the source region or between the source and the observer, will also modify the observed power-law spectrum[1].

Thermal Absorption

One mechanism giving rise to absorption is the scattering of thermal electrons by ions in the plasma. In such a scattering event, a photon may be emitted or absorbed as the electron is accelerated by coulomb field of the ion. In radio galaxies thermal emission is negligible compared to synchrotron emission. However, thermal absorption may significantly modify the radiation received from synchrotron sources within or behind the main body of the associated galaxy or from sources whose radiation must pass through ionized regions in our own galaxy. The optical depth due to absorption by thermal (electron) plasma is given by $\tau \sim L n_e^2 T^{-1.5} \nu^{-2.1}$, where L is the path length through the absorber, n_e is the thermal electron density and T is the temperature. Due to this increasing optical depth towards lower frequencies, thermal absorption will result in a turn-over or peak in the synchrotron spectrum observed at low frequencies. This turn-over happens at a frequency corresponding to $\tau = 1$.

Synchrotron Self-Absorption

If the intensity of synchrotron radiation within a source becomes sufficiently high, then re-absorption of the radiation through the synchrotron mechanism may become important. If it does take place, synchrotron self-absorption will drastically modify the spectrum of the source at low frequencies. Its spectral index below the turn-over frequency (ν_{SSA}) will be $+2.5$. Synchrotron self absorption is higher in small size radio sources.

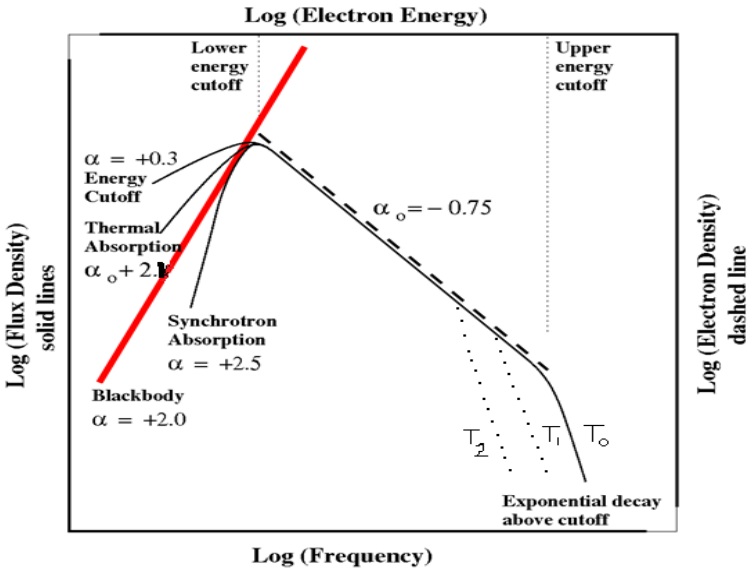

Figure 1.3: Figure shows the of Spectra of Radio sources. The x-labels above and below the figure are different but they share a correspondence (between Electron Energy and emitted Frequency). Similarly the y-labels on either side are related (Electron Density and Flux Density). The dotted line represents the electron energy power law. The high frequency steepening of spectrum with time is represented by the curves corresponding to the times $T_0 < T_1 < T_2$.

1.4 Ageing of Synchrotron electrons

The electrons lose energy through synchrotron emission and moves to lower energies with time. This decreases the upper energy cut-off resulting in a progressive steepening of spectra with time(as shown in Fig. 1.3). The time evolution of this break frequency ν_{break} (i.e. corresponding to the upper energy cut-off) is given by

$$\nu_{break} \simeq 3.4 \times 10^8 B^{-3} t^{-2} \tag{1.3}$$

where B is the magnetic field in the source region, measured in gauss and t is time in years.

1.5 Imaging with Giant Meterwave Radio Telescope (GMRT [11])

1.5.1 Radio Interferometry

Radio imaging has different practical issues as compared to optical imaging. The resolution of telescope is limited by diffraction, which is given by $1.22\lambda/D$, where D is the antenna dish size and λ is wavelength. The angular resolution of single radio antenna is insufficient for most astronomical purposes. Practical considerations limit the resolution to a few tens of arcsec. In radio astronomy, as the field of view is large (which is dependent on beam size, i.e., larger the beam size, larger the field of view), one has to deal with the Earth's curvature. To get high resolution (which can be obtained by having large antenna dish size) we use the technique of interferometry.

1.5.2 GMRT

GMRT is a radio interferometer array of 30 antennas, each with a diameter of 45 m. Its longest baseline (distance between 2 antennas) is $\sim$ 25 km. It can observe at 5 different frequencies bands, viz. 153, 233, 325, 610 and 1420 MHz. The angular resolution achieved is 10 arcsec at 325 MHz and scales with wavelength. It has a Y-shaped configuration of antennas. With GMRT we can achieve high resolution images due to its large baselines.

Chapter 2

Low Frequency Curvature

2.1 First Goal

We planned to put together a comprehensive set of radio data, comprising images at 74 - ([2]), 150 - (GMRT), 240 - (GMRT), 325 - (WENSS survey, Westerbork telescope, Netherlands, [10]) and 1400 - MHz (NVSS, Very Large Array, USA, [9]) MHz for several hundred galaxies. We selected these frequencies for our study, as we expect a deviation of the spectrum from a power-law. Of these, the 240 MHz GMRT data was observed and analysed by us at IISER. The rest, excluding GMRT 150 MHz, are available in public archives of other telescopes. The GMRT 150 MHz data has been observed as part of the TIFR-GMRT Sky Survey (TGSS) but has not yet been released to the public. We also have data from the Sloan Digital Sky Survey (SDSS) which is a public data base providing optical images, flux densities and colours of the galaxies in the entire northern hemisphere and part of the south. With this optical data we can have a more complete picture of the host galaxies of our radio sources.
In our study we planned to compare the low frequency spectra of normal galaxies and radio galaxies. In the normal galaxies as the emission is from within the disk of the galaxies, with its higher dust and thermal plasma content, the high thermal absorption is expected to affect the power-law spectra, as compared to that of double lobed radio galaxies where the thermal absorption is not so significant as the lobes are far from the galaxy.

There are several reasons of interest for observing at low frequencies $\sim$ 74 MHz [2] :-

1. Samples are completely dominated by isotropic radio emission, unlike those at higher frequency where orientation dependent Doppler boosting enhances the observed emission.

2. Spectral curvature is much more common at frequencies below 100 MHz than at higher frequencies.

3. Lower frequencies require lower electron densities.

Our main goal was to find out if there is any relation between the spectral curvature and

1. luminosity of the radio source ?

2. type of the optical galaxy ?

We also tried to find out the relative contributions of thermal absorption, synchrotron absorption or electron energy cut-off on the spectral curvature. All the 5 frequencies are essential for determining the spectra. Data at 240 and 150 MHz is essential in determining our spectral shape, as the spectral curvature occurs mostly near these low frequencies.

2.2 Imaging at 240 MHz using the GMRT

I imaged 53.625 $degree^2$ area of the sky in 11 overlapping fields of radius 2.083 degree near the North Galactic Pole (Fig . 2.1).

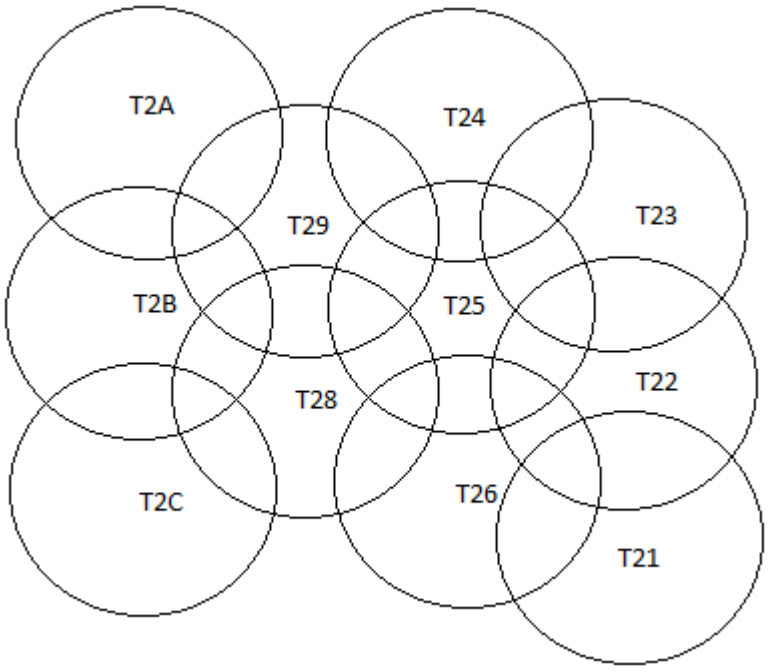

Figure 2.1: Schematic view of the Fields location

Field Name	Right Ascension(h:m:s)	Declination(d:m:s)
T21	12:21:30	33:00:00
T22	12:21:30	34:00:00
T23	12:21:30	35:00:00
T24	12:25:40	35:30:00
T25	12:25:40	34:30:00
T26	12:25:40	33:30:00
T28	12:29:30	34:00:00
T29	12:29:50	35:00:00
T2A	12:34:00	35:30:00
T2B	12:34:00	34:30:00
T2C	12:34:00	33:30:00

The images were made with the help of the software package *Astronomical Image Processing System* (AIPS) and the RFI recession software RfiX. A brief description of all the steps which were followed is given below.

Radio Frequency Interference(RFI)

RFI is the principle factor limiting the sensitivities of radio telescopes, particularly at low frequencies below 1 GHz. We used the software tool RfiX [3] to remove RFI from the data. It identifies RFI by detecting fringes in fringe-stopped correlator output.

Calibration

The purpose of calibration is to remove as far as possible, the effect of instrumental and environmental factors in the measurements. Such factors largely depend on the individual antennas or antenna pairs, so correction must be applied to the visibility data before they are combined into a map. For calibration we observe a strong source whose model structure we know, then calibrate the instrument. Generally we take point sources as model because its visibility function is simple (a constant). But in general point sources are not essential for calibration; any source whose actual structure is known can be used for calibration of the telescope. The desirable characteristics of a calibration source are the following :-
1) The calibrator should be strong enough, so that a good signal-to-noise ratio is obtained in a short observation.
2) The position of the calibrator should be close to that of the source being mapped : an angular distance no greater than 20 degrees in right ascension and 10 degrees in declination is desirable. Effects in the atmosphere that cause the gain to vary with pointing angle are then more effectively removed,

and time lost in driving the antennas between the map and calibrator is kept small.

In general we use both flux calibrator and phase calibrator for calibrating the source. Here, as the flux calibrator is nearby, we used it for phase calibration also. The calibrator been used for our calibration is 3C286.

Image Analysis

After the calibration, we carried out 5 rounds of standard imaging and phase-only self-calibration in AIPS. Subsequently we subtracted the sky model and flagged the bad data after inspecting the residuals. We reached our aim of $\sim$2 mJy/beam (1 mJy $\equiv$ milliJansky $= 10^{-29} W m^2 Hz^{-1}$) rms noise level in our images. The final cleaned images were corrected for the primary beam attenuation using the parameters specified on the GMRT webpage. We then detected all sources above 15 mJy using our source detection software programme.
We compared our list of sources for coincidence with sources listed in Cohen et al (74 MHz), NVSS and WENSS. This helped us in identifying spurious sources at 240 MHz which were detected in substantial numbers around very strong sources (>750 mJy) due to dynamic range limitations. We limited our project target selection to sources within a circle of radius 0.75 degrees around the centre of each field, as beyond this the noise level is $> 5mJy$ due to primary beam correction.
The resolution of the 240 MHz images is higher than that of WENSS and NVSS by a factor of 4 in each dimension. Therefore we carefully checked if multiple sources in the 240 MHz images corresponded to one or more sources in WENSS and NVSS. We also collected the data from SDSS (flux values at u,g,r,i & z bands), on the optical counterpart of the radio source. If there are more than one detections within 29 arcsec radius, then we took the nearest source as the possible source.

2.3 Results

A total of 116 sources with flux density $> 100mJy$ were selected for our analysis. We plotted spectra of each source and took only the sources with all 4 frequency data to finally check the change in spectral index from 325–1400 MHz to 74–240 MHz.

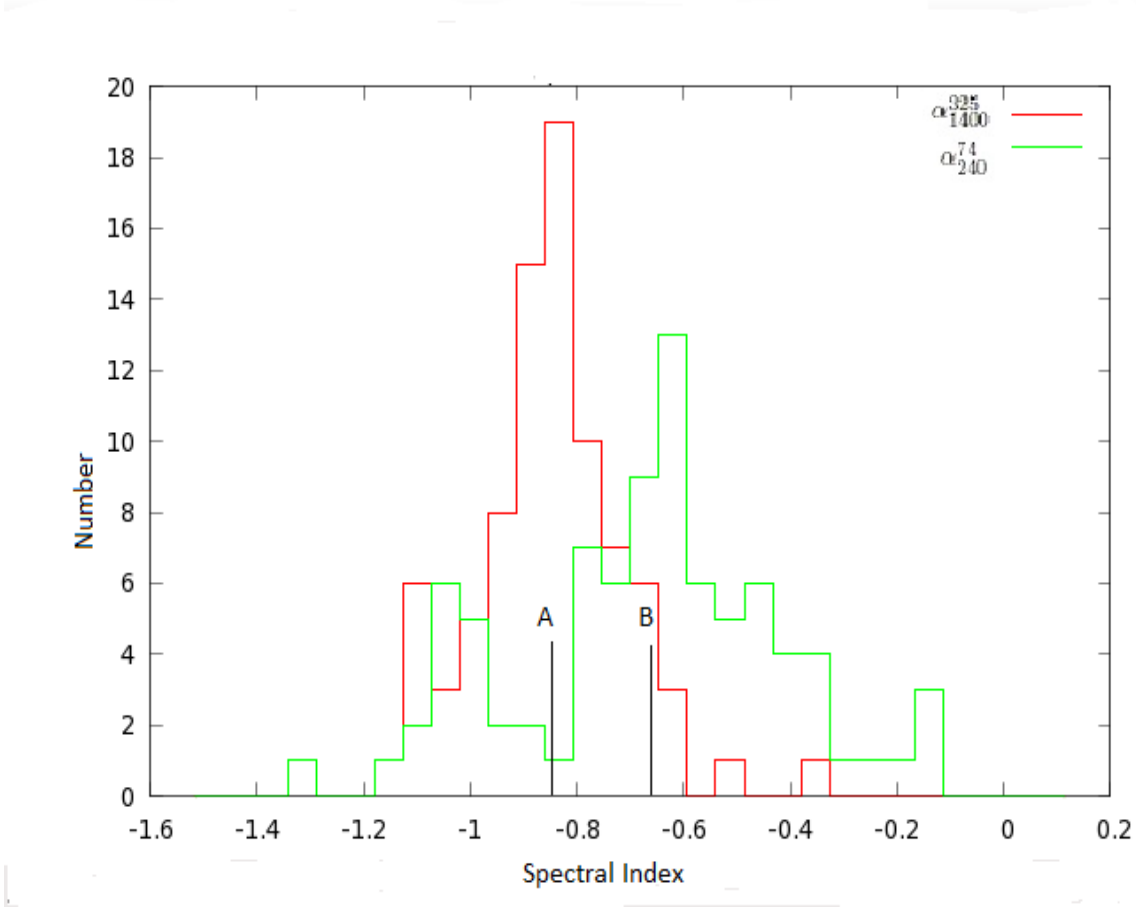

Figure 2.2: Histogram of α_{1400}^{325} and α_{240}^{74}, with their mean respective mean values at A= -0.8503 and B= -0.6635. Stating the steepening of spectra at higher frequencies

In the Fig. 2.2 we can see the shift in mean value of spectral index between 325 & 1400 MHz (given by A = -0.8503), and spectral index between 74 & 240 MHz (given by B = -0.6635). Clearly the mean values of spectral index show that spectra becomes flatter at lower frequencies. The details of all 116 sources are given in A.

As our fields overlapped at the half-power beam width point, some of the sources occurred in more than one field. For such sources we measured the parameters from the field in which the source was closest to the centre.

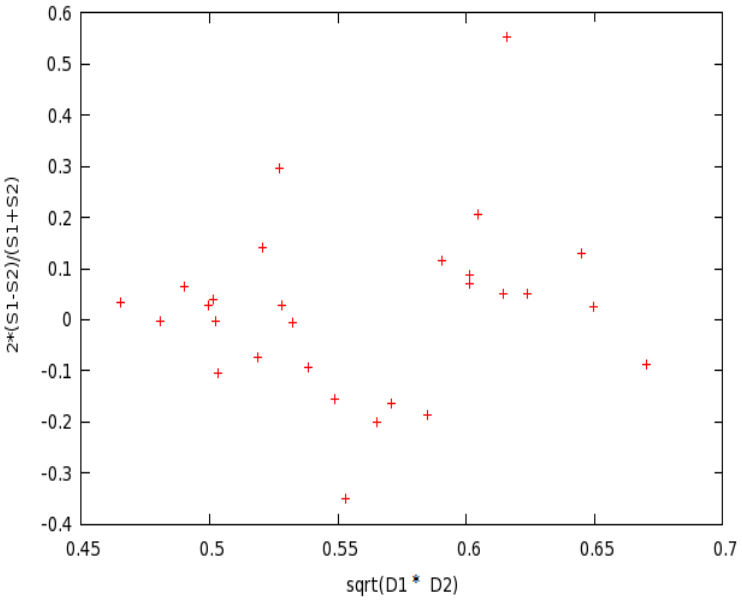

Figure 2.3: Plot of 2*(S1-S2)/(S1+S2) vs sqrt(D1*D2). Here S1-S2 signifies the difference in flux density of a particular source in two different fields. D1 and D2 are the source distance from centre of each respective field.

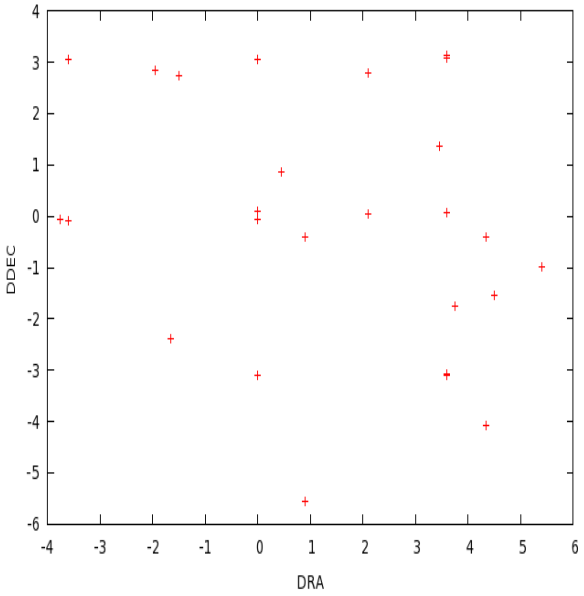

Figure 2.4: Plot of DRA vs DDEC for all the common sources.

The common sources also provided an opportunity to measure the positional

and flux density accuracy of the imaging exercise. Fig. 2.3 shows a plot of the normalised discrepancy between flux densities measured for the same source in two different fields. The geometric mean of the distances of the source to the centres of the two fields is plotted on the x-axis. The mean and 1σ dispersion for the normalised discrepancy are 0.000 and 0.11. The 10% error is within the flux density calibration error typical of such short observations.
Fig. 2.4 shows the plot of differences in right ascension (DRA) and declination (DDEC) of the positions of the common sources in different fields. The mean value & 1σ dispersion of DRA are 1.2214 & 2.6917 arcsec and that of DDEC are -0.0137 & 2.4483 respectively. For comparison, the pixel size in the images is 3.5 arcsec.

Table 2.1: Observation parameters of the GMRT 240 MHz imaging programme

Total Fields	11
Field Observation Day	20041205
Observation Time of each Field	8 min * 4 times = 32 min
Number of Antennas	30
Number of Baselines	435
Central Observation Frequency	241.9 MHz
Bandwidth of each baseline	8 MHz
Number of Channels in each Baseline	128
Number of Channels considered in each Baseline	94 (17-110)
Bandwidth of each Channel	62.5 KHz
Name of lta file from which Fields Observation Data Extracted	07rma01_ ngp.lta
Calibrator took for our Calibration	3C286

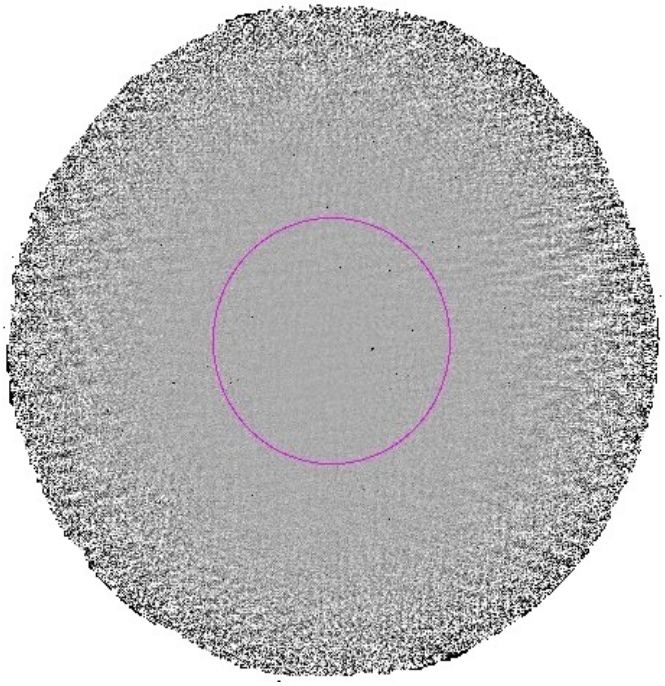

Figure 2.5: Image of a Field (T2C). Sources for our analysis were selected within the inscribed circle of 0.75 degree radius.

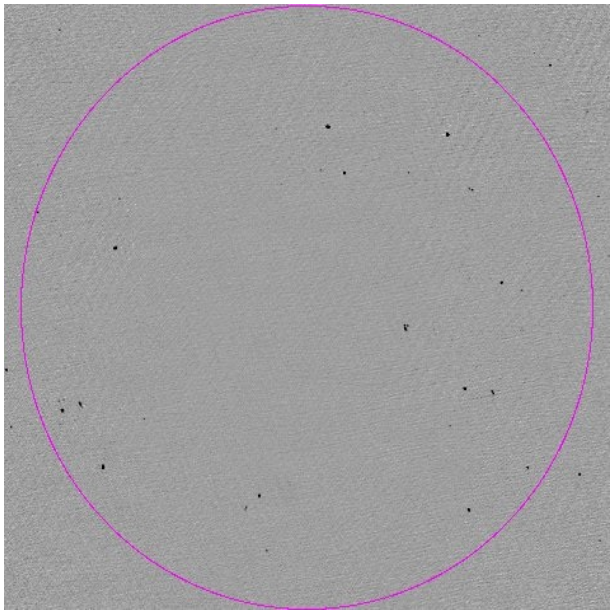

Figure 2.6: Image of a Field (T2C) within 0.75 degree radius

Unfortunately, as we could not get the 150 MHz data on time, without which it is difficult to do a proper low frequency spectral turnover analysis, as the 150 MHz frequency plays a vital role in determining the shape of the spectra. This led us to attempt an additional problem described in the next chapter. We expect to continue with this analysis once the 150 MHz data becomes available.

Chapter 3

Spectral Index of High Redshift Radio Galaxies

3.1 History

Whitfield (1957) first noted that higher redshift (in other words more distant) radio galaxies had steeper radio spectra. This was later confirmed by many people who have reported a correlation between spectral index (α) and either luminosity (L) or redshift (z) ([12], [8], [13]). It is known that in a flux density limited sample, there exists a strong correlation between L and z. Due to this strong correlation, there was a debate on whether the α primarily correlates with L or z. Initially, many investigators favoured an $\alpha - P$ correlation. However, Athreya & Kapahi, using a matched luminosity sample showed that higher red-shift (z>2) sources had a steeper spectrum than those at lower red-shift (0.85<z<1.7). Several reasons have been proposed for this.
Some of the proposed explanations for the observed correlations are:
α-z correlation
1. The denser medium at higher redshifts results in slower expansion of the radio source and therefore weaker shocks with fewer electrons accelerated to higher energies. This should result in steeper spectrum of injection of electrons and therefore steeper overall spectra[4]
2. Since the cosmic microwave background has a higher energy density at higher redshifts, high redshift galaxies will suffer a higher electron energy loss through the inverse Compton effect. Therefore, there spectra will become steeper at a faster rate with time, even if their initial electron injection spectrum is not different from that at lower redshifts.[7]
α-L correlation has been largely explained on the basis of a selection effect,

that high luminosity sources, which need to have large values of magnetic field will necessarily steepen faster as the ageing of electrons is also proportional to the magnetic field.
Athreya & Kapahi [4] compared a matched luminosity sample ($10^{28} - 10^{28.8}$ at 1 GHz rest frame) at intermediate ($0.85 < z < 1.7$) and high (z>2) redshifts. Using a range of frequencies they calculated the single-frequency spectral index between 1 GHz and 16 GHz in rest frame. They found that sources at higher redshifts have steeper spectra than intermediate redshifts, with a difference of $\sim$0.1 at 1 GHz rest frame (Fig. 3.1). Since the two samples had the same luminosity they argued that the correlation of spectral index was primarily with redshift. Since the spectral index difference did not change much between 1 GHz and 16 GHz they proposed that perhaps the difference will remain constant even at lower frequencies.
All other previous studies had argued that the electron injection spectrum (i.e. the spectral index at low frequencies, where the electrons have not had enough time to radiate sufficient energy and steepen their spectra) is the same at all redshifts and the difference in high frequency spectral index was due to faster radiation losses. Athreya & Kapahi were the first to propose that the electron injection spectrum itself may be steeper at high redshifts. However, the lowest frequency available for the analysis in [4] was 408 MHz in observed frame. This could not fully justify their suggestion of steeper electron injection spectrum at high redshifts, since the spectral index at 1 GHz could have been affected by curvature due to synchrotron losses. Since these are high redshift radio sources we needed to observe at much lower frequencies than 408 MHz (equivalent to rest frame 1 GHz) to determine the intrinsic electron injection spectrum.

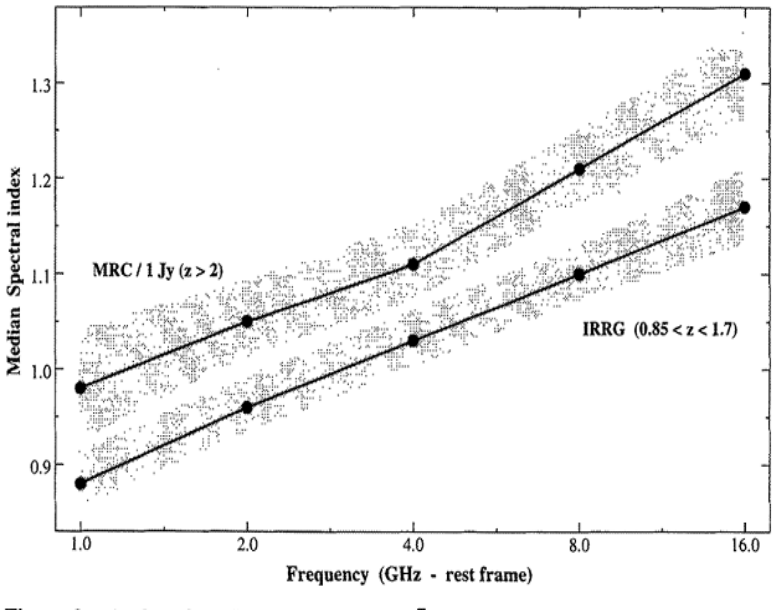

Figure 3.1: The plot of median spectral index (α_ν^T) versus frequency for the radio galaxy samples. The shaded area indicates the error on median values

3.2 This Project

Extensive data at 74, 150 and 325 MHz (observed frame) are now obtainable from public archives. Therefore, we decided to extend the work of Athreya & Kapahi to lower frequencies to check their hypothesis.
We compared 18 intermediate redshift sources from 3CRR listed in Athreya & Kapahi and compared it with with 24 sources at z $>$ 2 in Miley & De Breuck[6]. The sources selected all had observations at 74 MHz, 150-170 MHz, and 325-365 MHz. The sources were restricted to a luminosity range of $\log(L_{300MHz})$ = 28.4 - 29.3. We fitted a quadratic spectrum to the flux densities between 74 MHz and 365 MHz to obtain the single frequency spectral index and luminosity at 300 Mhz (rest frame). The data and the derived parameters are listed in Tables A.1 and A.2.
Figs. 3.2 and 3.3 shows representative spectrum including fit.

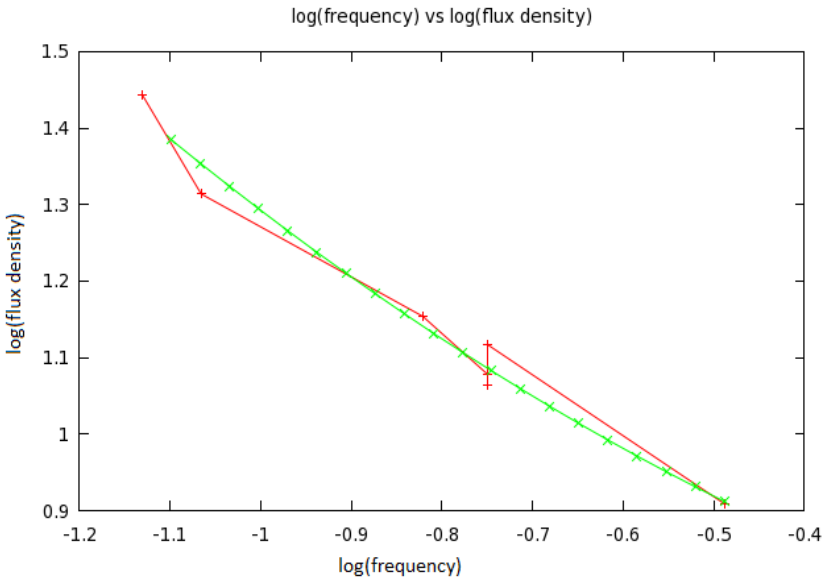

Figure 3.2: The plot of log(frequency) vs log(flux density). The green line shows the best fit

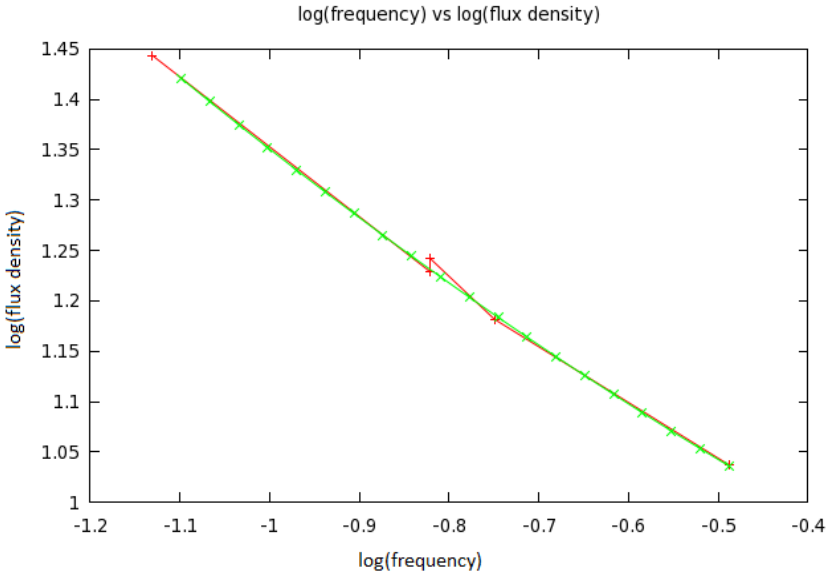

Figure 3.3: The plot of log(frequency) vs log(flux density). The green line shows the best fit

Spectral index, redshift and luminosity are plotted against each other in Figs.

3.4, 3.5 & 3.6.

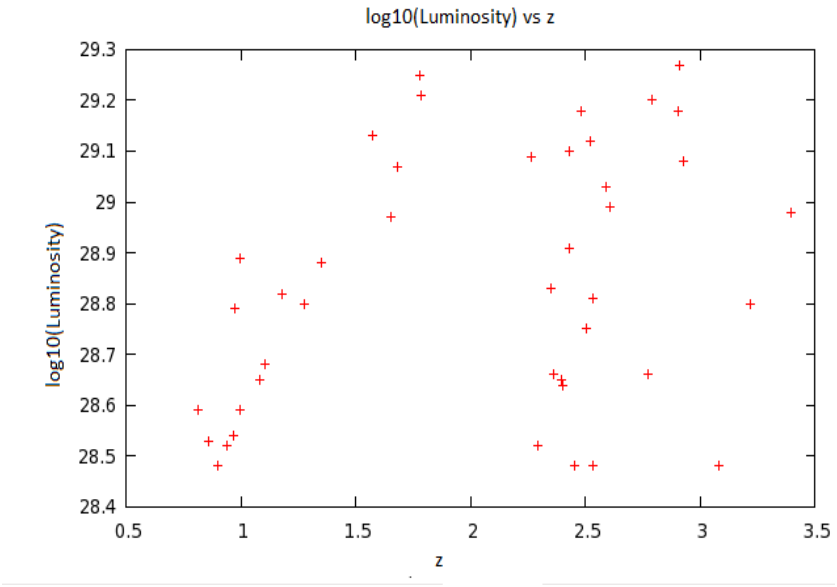

Figure 3.4: The plot of log10(Luminosity) vs redshift

By using two different flux limited samples we have eliminated the correlation between Luminosity and redshift as seen in Fig. 3.4. We can see some z-L relation at z<2 but none at higher redshifts, nor for the sample as a whole.

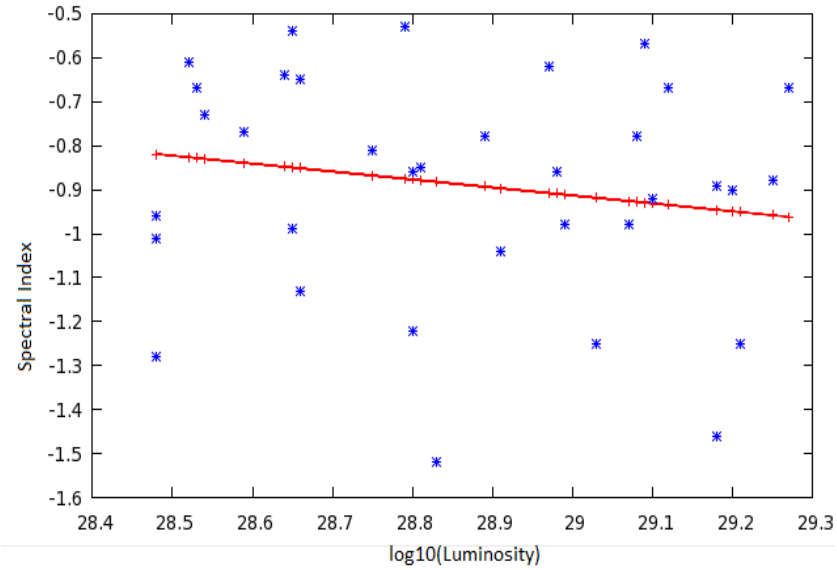

Figure 3.5: The plot of spectral index α vs log10(Luminosity). The red line shows the linear fit

In Fig. 3.5 we have plotted the data and a linear fit between spectral index α and log10(Luminosity). The best fit curve ($\chi^2 = 0.001$) is

$$\alpha = (-0.73 \pm 0.13) - (0.18 \pm 0.15)(log(L) - 28) \tag{3.1}$$

Though there is some correlation, it is not significant.

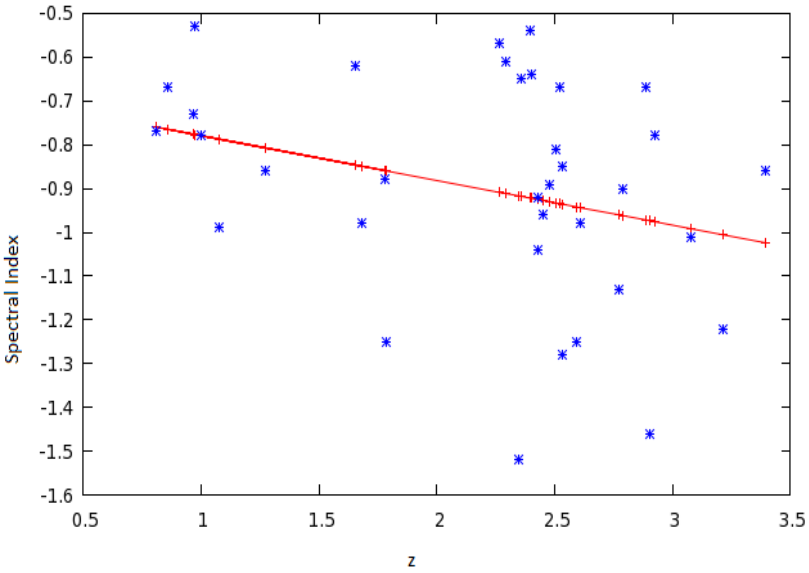

Figure 3.6: The plot of spectral index vs red-shift. The red line shows the linear fit

In Fig. 3.6 we have plotted the data and a linear fit between spectral index α and redshift (1+z). The best fit curve ($\chi^2 = 0.001$) is

$$\alpha = (-0.58 \pm 0.15) - (0.10 \pm 0.05)(1 + z) \tag{3.2}$$

The slope of spectral index with redshift is non-zero at the 2σ level and therefore is considerably stronger than dependence on luminosity.
A simultaneous linear fit between spectral index, luminosity (log(L)-28) and redshift (1+z) yielded the fit

$$\alpha = (-0.53 \pm 0.17) - (0.09 \pm 0.05)(1 + z) - (0.09 \pm 0.16)(log(L) - 28.0) \tag{3.3}$$

This once again suggests that there is no significant correlation between spectral index and luminosity but there is one between spectral index and redshift.
This analysis was done at 300 MHz frequency in rest frame. Which is low enough to state that spectral curvature due to synchrotron losses is not significant. The difference between the median redshifts of the two subsamples of Athreya & Kapahi was 1.2 and the difference in the spectral index was 0.1 at 1 GHz. Our best fit shows that a difference of 1.2 in redshift should translate to a difference of 0.11 in spectral index (at 300 Mhz) ... which is very similar to the difference at 1 GHz. Even though the overall spectral index at z = 2.38 has become flatter at 300 MHz compared to 1 GHz

($\alpha_{300M} = -0.83; \alpha_{1G} = -0.98$) the difference spectral index between high and intermediate redshift objects has been maintained. It may be noted that the $z > 2$ sample used in our analysis, collected from Miley & De Breuck, is substantially different from the sample used by Athreya & Kapahi. Yet, we have obtained very similar results. Therefore we conclude that at least some of the difference in spectral index is due to steeper electron injection spectrum at high redshifts.

The above analysis can be improved in two ways:

1. Clearly a larger data set would be welcome to improve the statistics
2. Some of the high redshift sources showed a substantial flattening in spectral index to values $\alpha > -0.5$. This flattening is much more likely to be due to spectral turnover due to absorption than due to a flat electron injection index. The known reduction in sizes of radio sources at high redshift may result in higher incidence of synchrotron self absorption and therefore a flattening of spectrum not associated with the electron injection spectrum. Therefore we did not use these sources in the analysis. However, a more careful analysis is essential taking into account the effect of linear sizes of radio sources before drawing any firm conclusion.

References

[1] Strong Non-thermal Radio Emission from Galaxies
Alan.T.Moffet (1972)

[2] A Deep,High-Resolution Survey at 74 MHz
A.S.Cohen, H.J.A.Rottgering, M.J.Jarvis, N.E.Kassim & T.J.W.Lazio
The AstroPhysical Journal Supplement Series, 150; 417-430 (2004)

[3] R.Athreya
The Astrophysical Journal,696:885-890,2009 May 1

[4] Redshift Dependence of Spectral Index in Powerful Radio Galaxies
Ramana M.Athreya & Vijay K.Kapahi
J.Astrophys.Astr. 19,63-77 (1998)

[5] On The Injection Spectrum of Relativistic Electrons in High Red-Shift Radio Galaxies
Gopal-Krishna, Mukul Mhaskey and A. Mangalam (2011)

[6] Distant radio galaxies and their environments
George Miley & Carlos De Breuck
Astron Astrophys Rev 15:67-144 (2008)

[7] Steep Radio Spectra in High-Redshift Radio Galaxies
Julian H.Krolik and Wan Chen
The Astronomical Journal, Volume 102, Number 5 (1991)

[8] Gopal Krishna, Wiita, P.J.
Astr. AstroPhys.,236, 305 (1990)

[9] Condon, J. J., Cotton, W. D., Greisen, E. W., Yin, Q. F., Perley, R. A., Taylor, G. B., & Broderick, J. J.
AJ, 115, 1693 (1998)

[10] Rengelink et al
A&A Suppl. 124, 259.(1997)

[11] Govind Swarup, Giant Metrewave Radio Telescope(GMRT), ASPC,1991.

[12] van Bruegel,W.,McCarthy,P.J. 1990 in *The evolution of galaxies*, ed. R. G. Kron (Hubble Centennial
Symp.,ASP Conf.Ser.10) page 359

[13] Chambers, K.C., Miley, G.K. 1990 in *The evolution of galaxies*, ed. R. G. Kron (Hubble Centennial
Symp.,ASP Conf.Ser.10) page 372

[14] C. De Breuck, Y Tang, A.G. de bruyn, H. Rottgering, W. van Breugel A& A 394, 56 (2002)

[15] A final non-reduntant catalogue for the 7C 151-MHz survey
S.E.G.Hales, J.M. Riley, E.M. Waldram, P.J.Warner and J.E.Baldwin
Mon. Not. R. Astron. Soc. 000,1-4(2007)

[16] The 6C survey of radio sources.
Haleales, S.E.G, Baldwin.J.E, Warner.P.J
Mon. Not. R. Astron. Soc., vol.234, p.919-936 (1988)

Appendix A

DATA

A.1 List of all the 116 sources taken for analysis of spectra

Table lists the co-ordinates, peak and flux values of all the 116 sources analysed.

	Right Ascension(h:m:s)	Declination(d:m:s)	Peak(mJy)	Flux(mJy)
	12:20:44.3	32:52:35.4	580	890
	12:20:41.5	33:10:02.4	660	741
	12:19:39.4	32:46:26.9	390	433
Field T21	12:20:18.9	32:42:58.7	125	230
	12:23:16.4	32:24:27.1	161	196
	12:23:14.2	32:22:12.2	61	114
	12:20:04.8	32:34:52.1	101	108
	12:20:55.0	33:31:35.7	54	106
	Right Ascension(h:m:s)	Declination(d:m:s)	Peak(mJy)	Flux(mJy)
	12:20:34.0	33:43:11.2	9285	15219
	12:22:41.7	34:19:37.7	266	496
Field T22	12:19:39.3	34:23:17.9	211	243
	12:20:42.4	33:47:26.4	178	189
	12:20:42.4	33:47:26.4	178	189

	Right Ascension(h:m:s)	Declination(d:m:s)	Peak(mJy)	Flux(mJy)
	12:19:44.8	35:34:09.2	1133	1363
	12:21:13.0	35:42:60.0	906	1148
	12:17:15.4	34:35:37.3	633	743
	12:16:50.6	34:44:21.9	442	702
	12:18:31.3	35:12:12.8	548	670
	12:18:17.9	35:48:26.7	109	319
	12:22:13.0	34:34:29.5	255	284
Field T23	12:16:49.7	34:55:00.8	132	275
	12:18:03.8	34:16:00.9	173	238
	12:20:08.2	34:31:22.2	194	230
	12:21:08.3	35:00:08.8	98	207
	12:23:30.6	35:06:59.2	102	195
	12:17:11.7	34:49:54.8	105	193
	12:17:33.2	34:49:57.6	162	189
	12:20:58.0	35:00:17.7	153	153
	12:20:00.3	35:31:09.9	73	104
	Right Ascension(h:m:s)	Declination(d:m:s)	Peak(mJy)	Flux(mJy)
	12:27:03.8	35:47:10.2	666	740
	12:27:58.7	36:35:10.3	543	631
	12:25:06.9	35:14:53.7	315	404
	12:30:33.0	35:40:52.9	341	389
	12:24:34.9	35:12:16.9	158	266
	12:28:14.0	36:37:15.2	229	249
	12:24:17.2	35:33:28.2	194	230
	12:29:49.1	36:11:29.2	134	208
Field T24	12:26:43.6	35:49:55.9	185	207
	12:26:25.2	36:41:26.8	150	165
	12:24:52.6	35:00:41.4	143	154
	12:25:33.2	34:44:44.9	139	151
	12:27:31.8	35:40:26.7	128	151
	12:26:07.5	35:29:26.8	119	126
	12:27:43.5	36:42:53.4	121	125
	12:27:44.0	35:45:32.0	94	111
	12:27:43.9	36:30:35.2	56	108

	Right Ascension(h:m:s)	Declination(d:m:s)	Peak(mJy)	Flux(mJy)
Field T25	12:23:27.0	34:38:04.5	210	319
	12:24:19.8	34:05:13.3	179	263
	12:24:10.9	34:05:00.9	141	182
	12:27:23.9	34:28:36.2	106	179
	12:25:26.7	34:02:50.9	139	159
	12:25:33.4	34:44:44.9	132	150
	12:23:18.9	34:23:42.9	78	102
	Right Ascension(h:m:s)	Declination(d:m:s)	Peak(mJy)	Flux(mJy)
Field T26	12:28:38.1	33:13:16.0	219	425
	12:25:05.3	33:56:17.7	204	240
	12:24:56.1	33:28:17.5	110	236
	12:24:10.7	34:05:04.0	135	173
	12:27:07.1	33:04:31.0	87	161
	12:26:40.8	32:59:29.0	70	127
	12:28:37.4	33:14:13.0	53	118
	12:25:29.0	33:01:29.9	64	112
	12:26:00.2	33:33:47.9	57	100
	Right Ascension(h:m:s)	Declination(d:m:s)	Peak(mJy)	Flux(mJy)
Field T28	12:30:10.5	34:29:23.6	587	628
	12:28:43.1	33:41:47.4	275	305
	12:30:06.0	34:04:20.6	192	205
	12:30:00.3	34:22:41.7	166	182
	Right Ascension(h:m:s)	Declination(d:m:s)	Peak(mJy)	Flux(mJy)
Field T29	12:27:04.3	35:47:08.1	599	794
	12:28:55.5	34:47:47.2	641	715
	12:28:51.9	34:56:41.1	437	531
	12:29:06.2	34:40:38.5	482	524
	12:30:33.3	35:40:50.5	375	390
	12:29:46.1	35:28:24.0	239	275
	12:28:23.1	35:27:22.1	218	248
	12:30:10.1	35:10:20.9	80	160
	12:28:09.4	34:47:15.4	94	151
	12:29:22.3	35:55:29.9	99	145
	12:30:36.7	35:32:05.4	116	139
	12:28:43.3	34:44:40.8	70	136

	Right Ascension(h:m:s)	Declination(d:m:s)	Peak(mJy)	Flux(mJy)
Field T2A	12:35:07.9	35:53:16.8	340	735
	12:37:20.8	35:26:55.6	534	566
	12:30:36.8	36:04:52.4	193	461
	12:32:32.8	35:44:19.0	364	434
	12:34:23.8	36:08:59.9	270	299
	12:34:08.4	35:25:26.9	257	296
	12:37:01.4	35:57:57.5	105	237
	12:36:03.0	35:16:02.0	80	236
	12:33:24.4	35:59:05.7	60	192
	12:33:16.3	35:00:50.4	127	153
	12:37:17.9	35:57:01.9	120	137
	12:36:14.8	35:54:01.3	53	120
	12:33:18.5	36:26:53.7	109	120
	12:31:16.6	36:05:23.2	91	118
	12:35:05.8	36:21:14.0	96	111

	Right Ascension(h:m:s)	Declination(d:m:s)	Peak(mJy)	Flux(mJy)
Field T2B	12:32:41.4	34:42:52.4	1880	2793
	12:34:04.6	34:48:54.0	313	368
	12:33:28.4	34:39:50.7	110	183
	12:35:08.8	34:37:52.8	106	131
	12:33:28.6	34:51:20.7	100	111
	12:37:27.3	34:47:52.1	81	101

	Right Ascension(h:m:s)	Declination(d:m:s)	Peak(mJy)	Flux(mJy)
Field T2C	12:32:13.0	33:55:42.1	1144	1110
	12:33:43.1	33:56:53.9	402	670
	12:36:24.4	33:38:48.7	339	593
	12:32:00.8	33:17:47.4	442	491
	12:38:45.3	33:14:21.5	231	457
	12:33:01.4	32:35:22.9	378	432
	12:32:45.5	33:26:43.6	256	422
	12:33:31.4	33:49:59.8	359	362
	12:37:04.1	33:14:24.4	254	339
	12:36:32.8	33:05:57.1	138	252
	12:31:58.2	32:59:41.2	186	236
	12:31:32.6	33:33:36.5	185	190
	12:31:40.3	33:17:22.0	45	127
	12:34:35.5	33:01:59.6	68	121
	12:30:34.7	33:04:55.3	100	120
	12:33:48.6	32:44:08.9	81	112
	12:37:56.1	32:55:24.8	80	104

A.2 List of the 42 sources along with their flux values took for $\alpha - z$ correlation

Table lists all the 42 sources along with their corresponding redshifts and flux values(at different observational frequencies). Here S1, S2, S3, S4, S5,S6 and S7 represents flux densities at 365 - (NASA/IPAC EXTRAGALACTIC DATABASE (NED)), 325 - (WENSS [10]/ WISH([14])), 178 - (NED), 160 - (NED), 151 - (7C [15], 6C [16]), 80 - (NED), 74 - (Cohen [2]) MHz respectively. The flux values are given in mJy.

Source	z	S1	S2	S3	S4	S5	S6	S7
3CR13	1.351	—-	8109	13080/ 11600/ 12000	—-	14255	20600	27800
3CR22	0.937	—-	8593	13189/ 12100/ 10900	—-	17140	25300	22790
3CR65	1.176	—-	10892	15200	—-	17450/ 16940	—-	27780
3CR68.2	1.5753	—-	3124	13000/ 14170/ 10000	15800	12130/ 12750	32500/ 28000	29540
3CR184	0.994	—-	9676	11800/ 13200/ 14388	—-	14870/ 15200	23800	23660
3CR217	0.898	—-	8970	12317/ 11300/ 14500	—-	16498	24400	25380
3CR252	1.104	—-	6933	11000/ 10800/ 11990	15600	13680	31400/ 26000	31520
3CR266	1.275	—-	6932	11100/ 12099/ 10400	—-	13914	22800	23070
3CR268.1	0.974	—-	17620	23000/ 21400/ 20700/ 22130/ 23326	—-	25290/ 25700	43000	30870
3CR280	0.998	—-	16888	23700/ 25833/ 26300/ 25350	—-	36480/ 29880	45000	51760
3CR289	0.967	—-	8796	11800/ 12000/ 13080	—-	16240	21100	26400
3CR322	1.681	—-	7634	10100/ 10200/ 11009	—-	12900/ 12700	25400	22270

continuation.....

3CR325	0.860	—-	12594	17004/ 15600/ 14500	—-	19150/ 19160	33100	30410
3CR356	1.079	—-	7185	11300/ 12317	—-	13980/ 14060	26300	28950
3CR470	1.653	—-	6904	10100/ 11009/ 9000	—-	11700/ 11790	14700	18630
3CR239	1.781	—-	8534	13200/ 13000/ 14388	—-	18060/ 18030	25800	31570
3CR265	0.811	—-	15601	18300/ 19500/ 21255	27900	24150	42100/ 50000	46460
3CR294	1.786	—-	6776	10300/ 11227	15700	13330	27900/ 31000	31030
4C 40.36	2.265	3173	3394	7000	—-	6460	—-	11230
1106+380	2.290	—-	1368	—-	—-	1994	3290/ 2770	
TXS 1707+105	2.349	1374	—-	2200	—-	—-	—-	6990
4C -00.54	2.360	948	—-	2000	—-	—-	—-	3840
0930+389	2.395	1061	1161	—-	—-	2500/ 2210	—-	3750/ 3480
4C 34.34	2.400	1391	1515	2100	—-	2310	—-	3620
4C 40.02	2.428	1329	1560	2700	—-	3414	—-	6880
B3 0731+438	2.429	2850	3403	4500	—-	5910/ 5890	—-	10610
8C 1536+620	2.450	—-	680	—-	—-	1289	—-	2490
4C 23.56	2.479	1991	—-	4200	6500	—-	12000/ 13000	10110
WN J0303+3733	2.505	954	1071	—-	—-	2500/ 2200	—-	4300
TXS 1558-003	2.520	1770	—-	4300	5400	—-	10000/ 9000	9100
8C 1039+681	2.530	1150	1254	—-	—-	2628	—-	4830
0112+372	2.535	491	518	—-	—-	1030	—-	2390
TXS 2353-003	2.592	1476	—-	2900	—-	—-	—-	8060
4C 26.38	2.609	736	—-	3300	2900	1630	15000/ 14000	3800/ 3240

continuation.....

WNR J1338+3532	2.772	647	723	—-	—-	1340	—-	2840
4C +44.02	2.790	2382	—-	3600	—-	5670/ 5370	—-	9310
4C 24.28	2.889	2742	—-	4800	6600	5940	9000/ 10000	10760
4C 28.58	2.905	1649	—-	2900	—-	—-	—-	8550
B3 0744+464	2.926	2004	—-	3100	—-	3860/ 3820	—-	6360
WNJ0231+3600	3.080	—-	303	—-	—-	690	—-	1440
WNJ1123+3141	3.216	525	623	—-	—-	1190	—-	2670
B2 0902+34	3.395	1118	1213	—-	—-	2060	—-	3650

A.3 List of 42 sources along with their parameter values took for $\alpha - z$ correlation

Table lists all the 42 sources, their quadratic fit parameters $A_0, A_1 \& A_2$, α and log(Luminosity). Here both α and Luminosity are measured at 300 MHz in rest frame.

Source	z	A_0	A_1	A_2	α	log(Luminosity)
3CR13	1.351	0.7005	-0.2820	0.3102	-0.84	28.88
3CR22	0.937	0.5784	-0.6727	0.0498	-0.75	28.52
3CR65	1.176	0.8141	-0.3763	0.1603	-0.65	28.82
3CR68.2	1.575	-1.1098	-4.0718	-1.5692	-1.14	29.13
3CR184	0.994	0.8021	-0.2420	0.2520	-0.66	28.59
3CR217	0.898	0.6894	-0.4261	0.1974	-0.74	28.48
3CR252	1.104	0.4899	-0.5469	0.3129	-1.08	28.68
3CR266	1.275	0.4113	-0.8710	-0.0080	-0.86	28.80
3CR268.1	0.974	1.0332	-0.3501	0.1092	-0.53	28.79
3CR280	0.998	0.8566	-0.7200	0.0350	-0.78	28.89
3CR289	0.967	0.7269	-0.3119	0.2564	-0.73	28.54
3CR322	1.681	0.7486	0.0021	0.5153	-0.98	29.07
3CR325	0.860	1.0401	0.1548	0.5187	-0.67	28.53
3CR356	1.079	0.5681	-0.4143	0.3445	-0.99	28.65
3CR470	1.653	0.5150	-0.6781	-0.0284	-0.62	28.97
3CR239	1.781	0.4908	-0.8886	-0.0039	-0.88	29.25
3CR265	0.811	1.1687	0.3095	0.6921	-0.77	28.59
3CR294	1.786	0.5609	-0.2917	0.4932	-1.25	29.21
4C 40.36	2.265	-0.0858	-1.5236	-0.4617	-0.57	29.09
1106+380	2.290	-0.0394	-0.2839	0.1550	-0.61	28.52
TXS 1707+105	2.349	0.1643	0.4778	0.9546	-1.52	28.83
4C -00.54	2.360	-0.6185	-1.5473	-0.4277	-0.65	28.66
0930+389	2.395	-0.5411	-1.4748	-0.4446	-0.54	28.65
4C 34.34	2.400	-0.0699	-0.4605	0.0841	-0.64	28.64
4C 40.02	2.428	-0.3010	-0.9748	0.0290	-1.04	28.91
B3 0731+438	2.429	0.2306	-0.4543	0.2219	-0.92	29.10
8C 1536+620	2.450	-0.5057	-0.6133	0.1629	-0.96	28.48
4C 23.56	2.479	-0.4307	-1.8418	-0.4453	-0.89	29.18
WN J0303+3733	2.505	-0.5607	-1.3375	-0.2486	-0.81	28.75
TXS 1558-003	2.520	-0.5674	-2.1616	-0.6983	-0.67	29.12
8C 1039+681	2.530	-0.3911	-1.0645	-0.1002	-0.85	28.81
0112+372	2.535	-0.5093	-0.2320	0.4894	-1.28	28.48
TXS 2353-003	2.592	-0.1365	-0.5565	0.3234	-1.25	29.03
4C 26.38	2.609	-1.1328	-2.5842	-0.7438	-0.98	28.99
WNR J1338+3532	2.772	-0.4209	-0.3973	0.3319	-1.13	28.66
4C +44.02	2.790	0.0027	-0.8194	0.0377	-0.90	29.20
4C 24.28	2.889	-0.0460	-1.2068	-0.2393	-0.67	29.27

continuation .....

4C 28.58	2.905	0.0841	-0.0226	0.6431	-1.46	29.18
B3 0744+464	2.926	0.0157	-0.6148	0.0746	-0.78	29.08
WNJ0231+3600	3.080	-1.0752	-1.1727	-0.0723	-1.01	28.48
WNJ1123+3141	3.216	-0.5497	-0.5182	0.3041	-1.22	28.80
B2 0902+34	3.395	-0.1950	-0.4900	0.1588	-0.86	28.98